Turkish Journal of Electrical Engineering & Computer Sciences

http://journals.tubitak.gov.tr/elektrik/

Research Article

Turk J Elec Eng & Comp Sci
(2014) 22: 1517 – 1527

doi:10.3906/elk-1105-58

Study on interior permanent magnet synchronous motors for hybrid electric vehicle traction drive application considering permanent magnet type and temperature

Javad SOLEIMANI[1,*], Abolfazl VAHEDI[2], Abdolhossein EJLALI[2], Mohammadhossein Barzegari BAFGHI[2]

[1]Young Researchers and Elites Club, Hamedan Branch, Islamic Azad University, Hamedan, Iran
[2]Electrical Engineering Department, Iran University of Science & Technology, Tehran, Iran

Received: 01.06.2011 • **Accepted:** 07.02.2013 • **Published Online:** 07.11.2014 • **Printed:** 28.11.2014

Abstract: Recently, interior permanent magnet synchronous motors (Interior-PMSMs) have become known as a good candidate for hybrid electric vehicle (HEV) traction drive application due to their unique merits. However, the dynamic and steady-state behaviors of these motors are quite dependent on the permanent magnet (PM) type, configuration, and volume in rotor structures. This paper uses a novel structure of Interior-PMSMs for traction applications with fragmental buried rotor magnets in order to achieve low torque ripple, iron losses, and cogging torque. In this paper, first, the effect of the PM type on a d-q equivalent circuit model is examined. Next, the design and simulation of an Interior-PMSM for HEV traction drive application, in order to extract the output values of the motor and sensitivity analysis of the PM type, are done using a 3-dimensional finite element method model. We then present the back electromotive force, power factor, cogging torque, flux density, torque per ampere diagram, PM volume, and constant power speed ratio value behavior of the designed Interior-PMSM with different PMs in the rotor structure, and we discuss the effect of temperature variation on these output parameters. This study can help designers in the design approach of such motors.

Key words: Permanent magnet, Interior-PMSM, 3D-FEM model, traction, temperature analysis

1. Introduction

The main features of interior permanent magnet synchronous motors (Interior-PMSMs) for hybrid electric vehicle (HEV) traction drive applications are simple construction with conventional 3-phase stator windings, with low current density and a rotor with inner fragmental permanent magnets (PMs) [1–5]. Interior-PMSMs have little volume, light weight, high efficiency and power factor, and high reliability; these advantages make the Interior-PMSMs especially suitable for HEV applications [6,7]. Interior-PMSMs use the hysteresis characteristics of magnetic materials; it is known that the efficiency, back electromotive force (EMF), power factor, and torque behavior of these motors could be easily affected by the type, temperature [8–10], volume, and configuration of PMs [11–15]. In these studies, the effect of different PMs on motors has been considered with a constant volume of PMs; therefore, the resultant back EMF will be variable and this strategy is not appropriate for the optimal design of different motors. In this paper, the best designs with different PMs are carried out by constant back EMF and a variation of the PM volume in all of the prototype designs, and the performance and temperature effects are also studied for prototype motors. Thus, the effect of different PMs in the rotor structure on back

*Correspondence: jsoleimani@iauh.ac.ir

EMF, power factor, cogging torque, flux density, torque per ampere diagram, PM volume, and constant power speed ratio (CPSR) behavior of an Interior-PMSM, as well as the effect of the PM type on a d-q equivalent circuit model, are investigated. Meanwhile, the finite element method (FEM) is implemented for accurate simulation. This 3-dimensional FEM (3D-FEM) model has a high level of accuracy and gives better insight about the motor performance. Finally, the objective of this paper is to derive the performance characteristics of Interior-PMSMs and perform a sensitivity analysis of such motors at synchronous speeds based on the 3D-FEM model. It is clear that the effect of increasing the temperature on the insulators and PM is greater than on other parts of the Interior-PMSM [15], but by choosing an F-class insulator, the damaging effect of increasing the temperature on the insulators will be decreased. This study discusses the effect of temperature variation on the hysteresis loop characteristics of PMs. Moreover, this model can be used in the design approach and precise analysis of an Interior-PMSM for HEV traction applications.

2. Structure and winding configuration

As shown in Figure 1a, an 80-kW Interior-PMSM with 8 poles, 48 slots, and 6 slots per pole, for possible HEV application, is designed with 3 layers of fragmental buried rotor magnet in order to achieve the maximum torque per ampere, and all of these layers have a trapezoid structure, as shown in Figure 1b, for reduced hot spots [5] (zones that have maximum flux density).

In this machine, a kind of PM material in the rotor structure is used that has suitable reversible temperature coefficients, as can be seen in Table 1 [10]. Moreover, laminations of the soft magnetic material (permendur-24) for constructing the stator and rotor cores, and a kind of stainless steel with very low relative permeability in the shaft structure, are used. The permendur-24 characteristics are given in Table 2 [16].

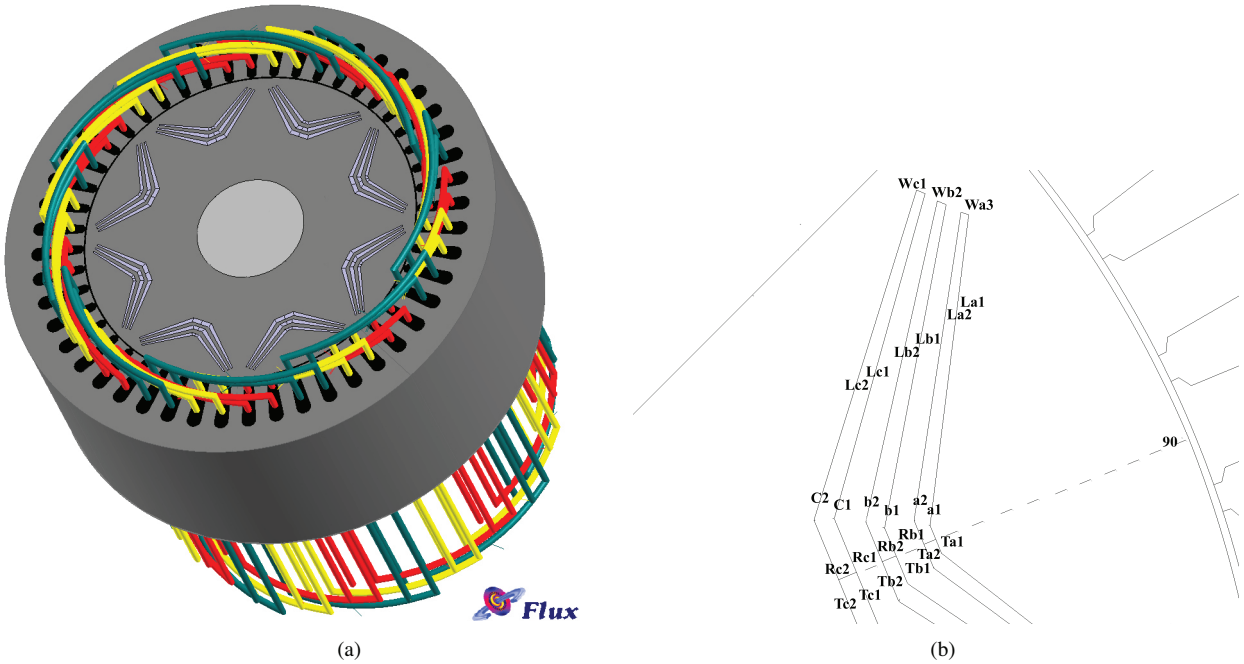

(a) (b)

Figure 1. a) The 8-pole, 48-slot Interior-PMSM structure for traction application with 3 layers of fragmental buried rotor magnets; b) novel structure of the rotor.

The stator slots are embedded with double-layer fractional-slot (5/6) windings, with 18 conductors per stator slot and each phase, and requiring 8 turns of the windings to achieve harmonic reduction. The current density in the windings is 4.2 A/mm^2 and the radius of each naked wire is 2.936 mm, using F-class insulators. The winding diagram and the terminal connection mode of the 8-pole stator winding are shown in Figures 2a and 2b. Analysis of the model is performed at one-half pole by 3D-FEM.

Table 1. PM characteristics.

Parameters	B_r (T)	H_c (KA/m)	$_r\mu$	T_{max} (°C)	T_{cure} (°C)	T_c of B_r	T_c of H_c	Prototype
Bonded Sm_2Co_{17}	0.7	416	1.1	80	725	–0.08	–0.04	No. 1
Bonded Nd-Fe-B	0.68	460	1.25	150	340	–0.1	–0.6	No. 2
Sintered Sm_2Co_{17}	1	820	1.05	300	750	–0.08	–0.3	No. 3
Sintered Nd-Fe-B	1.41	1500	1.07	180	310	–0.1	–0.6	No. 4

Table 2. Soft magnetic material characteristics.

Parameters	Saturation flux density (T)	Remanence (T)	Initial permeability	Maximum permeability
Permendur 24	2.34	1.5	250	2000

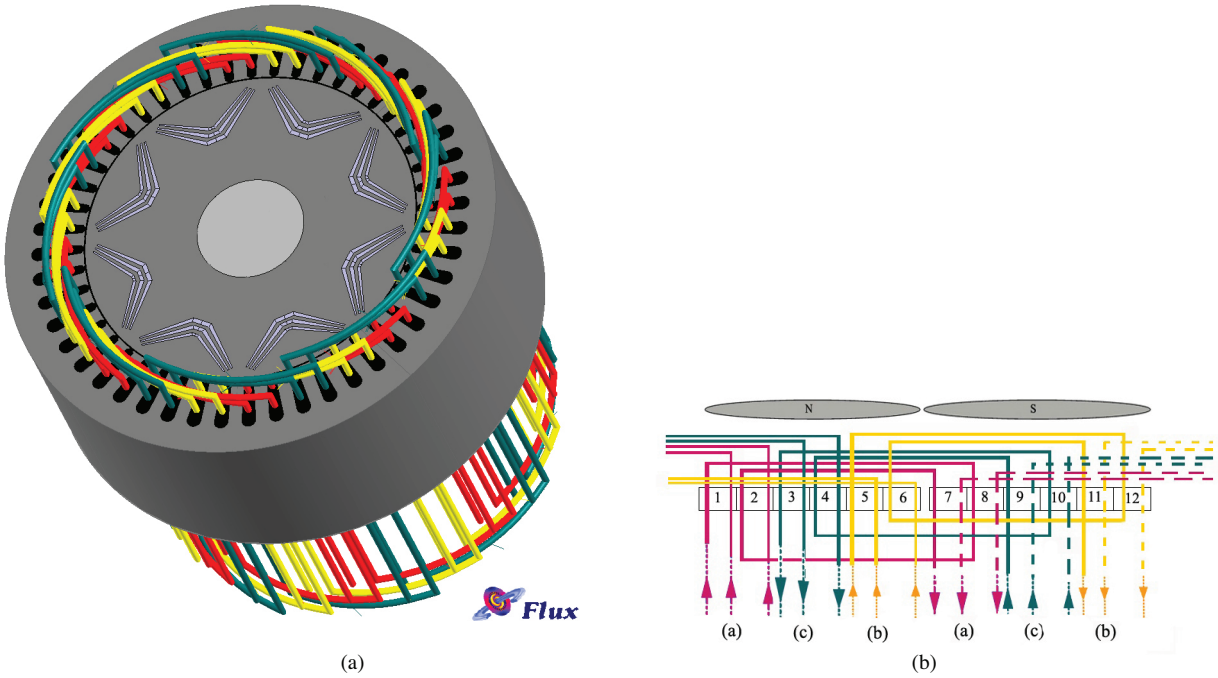

(a) (b)

Figure 2. a) Winding diagram and b) stator terminal connection of the 8-pole Interior-PMSM with double-layer distributed windings.

3. FEM model

As mentioned previously, a 3D-FEM model, which gives better insight about the motor performance, is implemented in order to simulate the proposed motor.

In order to have a high level of accuracy, the automatic mesh diagram is not used and a mesh diagram is designed manually, where the node congestion is higher around the air gap. The total number of nodes is about 190,000, which leads to high accuracy. Meanwhile, for boundary conditions, the homogeneous Dirichlet condition is adopted on the infinite box that encompasses the motor.

This simulation is based on a circuit-coupled model using the phase voltage as input. Figure 3 shows the circuit-coupled model used in this study, where for each phase, 8 coil windings are considered, and of those, 4 coils are sent to the current in the motor and 4 coils return current from the midpoint of the winding in the star connection. The coil winding connection in each phase is exactly as illustrated in Figure 2b.

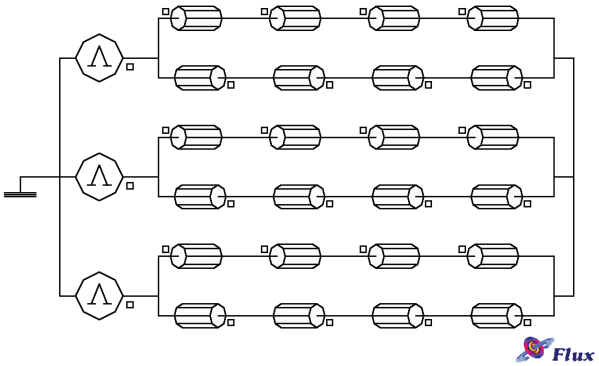

Figure 3. Circuit-coupled model used in the simulation.

4. PM volume

In this study, complex permeability (the rhombus shape hysteresis loop) is used. Figure 4 helps to exploit this hysteresis loop. In order to choose an accurate volume of PM regarding the magnetic circuit that the PM material is in, an iteration method is used, which is illustrated by a flowchart in Figure 5. In the first iteration for each type of PM, the volume is obtained by:

$$V_m = \frac{c_v.P_{out}}{F.B_r.H_c}. \tag{1}$$

Here, C_v is a coefficient that depends on the PM design in the rotor structure and is approximated at between 0.54 and 3.1 [5,9]. From the finite element analysis, the back EMF in each phase can be obtained and checked with the amplitude of the input voltage in each phase, and this procedure continues until the convergence criterion is satisfied. As can be observed from the simulation results, this procedure is also effective for choosing the PM volume with complex permeability.

5. PM hysteresis loop effect on d-q equivalent circuit model

Figure 6 shows the d-q-0 equivalent circuit model of a PMSM [5,17–21]. It is proven that variation of the PM hysteresis loop characteristics has an effect on the equivalent magnetizing current and inductance of the excitation axis (d-axis). The magnetic circuit of a PM and its equivalent electrical circuit are shown in Figures 7a and 7b, respectively. The equations below show the effect of the PM on those terms:

$$P_{rc} = \frac{l_m}{\mu_0 \mu_r A_m}, \tag{2}$$

$$F_0 = H_c.l_m, \tag{3}$$

and the magnetic flux of the PM is obtained by:

$$\varphi_r = B_r A_m. \tag{4}$$

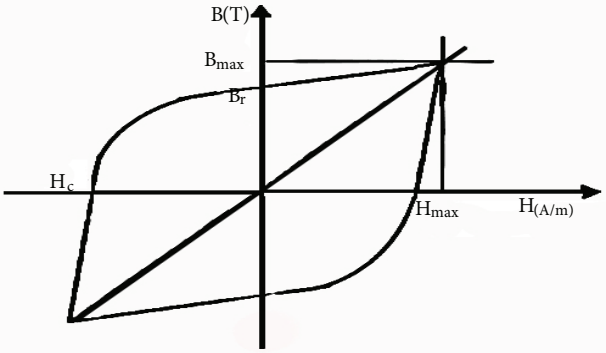

Figure 4. Inclined hysteresis loop approximation.

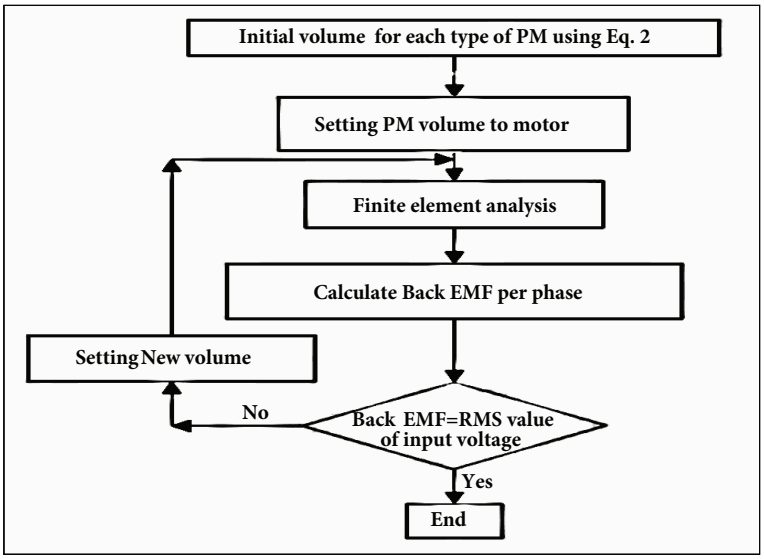

Figure 5. Flowchart for accurate volume of the PM selection.

Here, l_m and A_m, respectively, are the length and pole cross-section of the PM, and μ_0 and μ_r respectively denote the permeability of the free space and relative permeability of the PM. This equivalent electrical circuit is combined with the excitation axis of the d-q equivalent circuit model of PM synchronous machines. Variations of the PM remanent flux density, coercive field strength, and relative permeability while considering the PM's temperature variation are shown in Figures 8a–8c, respectively.

6. Results and discussion

Based on the above aspects, finite element simulation for the Interior-PMSM is performed. The simulation research is made for an 8-pole Interior-PMSM prototype. The parameters of the Interior-PMSM prototype and the output quantities of the motor for a 1.6-mm air gap are given in Table 3. It must be noted that half of one pole is analyzed because of the magnetic symmetry of the motor. As seen in Figure 9, node congestion becomes

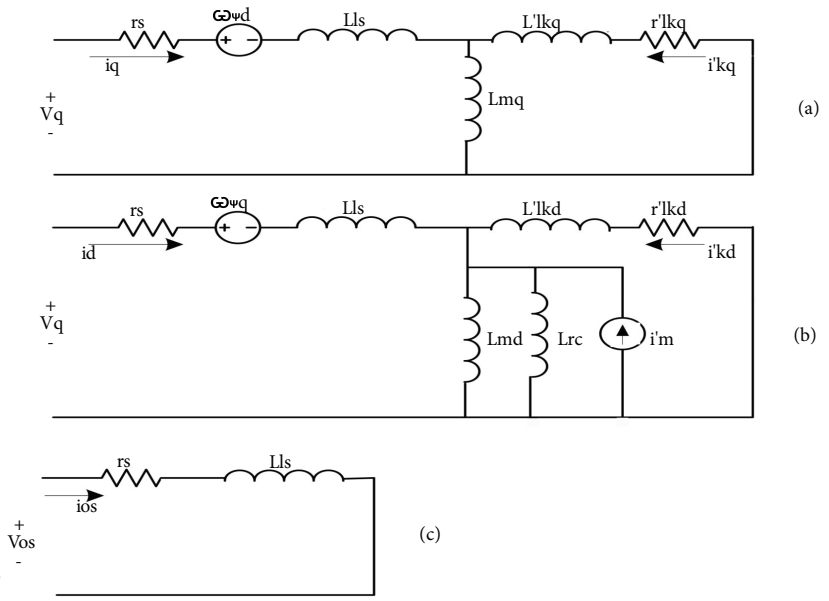

Figure 6. The d-q-0 equivalent circuit model of the PMSMs: a) q-axis, b) d-axis, c) 0-sequence.

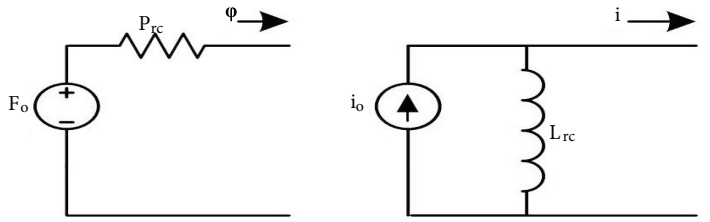

Figure 7. The PM's equivalent circuits: a) magnetic circuit, b) electrical circuit.

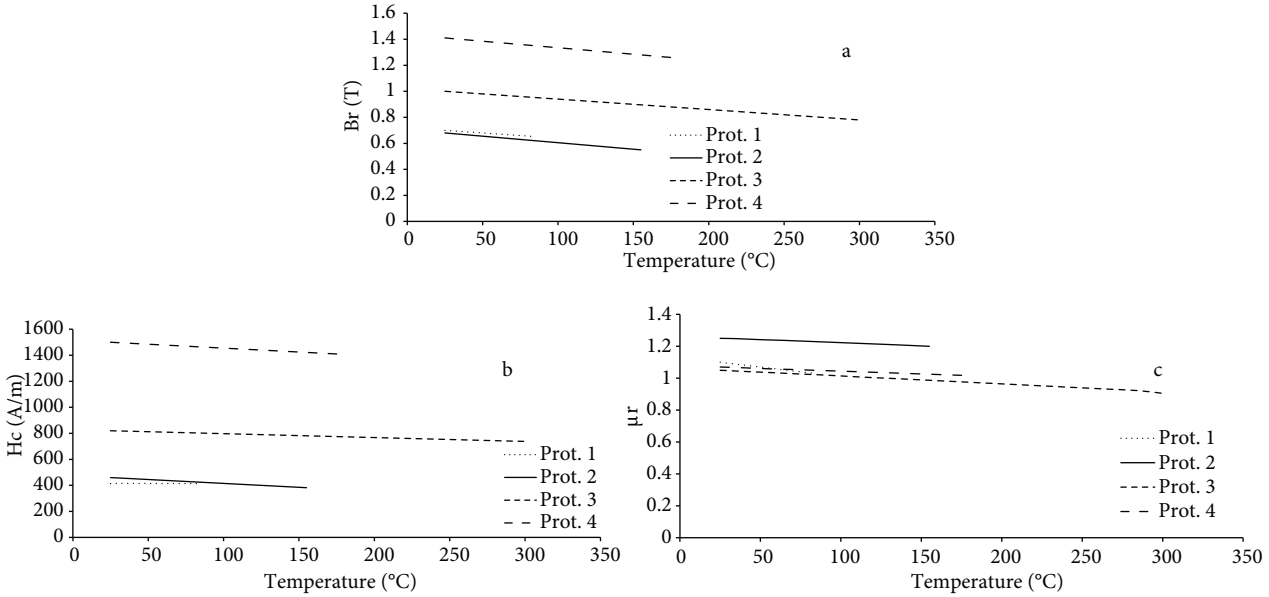

Figure 8. Effect of temperature variation on the PM hysteresis loop characteristics: a) remanent flux density, b) coercive field strength, c) relative permeability.

higher near the air gap in order to ensure accuracy of the simulation. Based on the FEM model, the simulation of all of the prototypes for real dimensions is performed and the output characteristics are extracted.

Table 3. Motor features.

Quantity	Value	Quantity	Value
Rated voltage (V)	900	Outer diameter of the stator (mm)	734
Rated power (Kw)	80	Inner diameter of the stator (mm)	498
Frequency (Hz)	50	Stator stack height (mm)	560
Speed (rpm)	750	Type of winding	Concentric with consequent poles
Phase connection	Y	Number of turns per slot	20
Pole pairs	4	Core material (stator and rotor)	Permendur-24
Number of stator slots	48	Air gap length (mm)	1.6

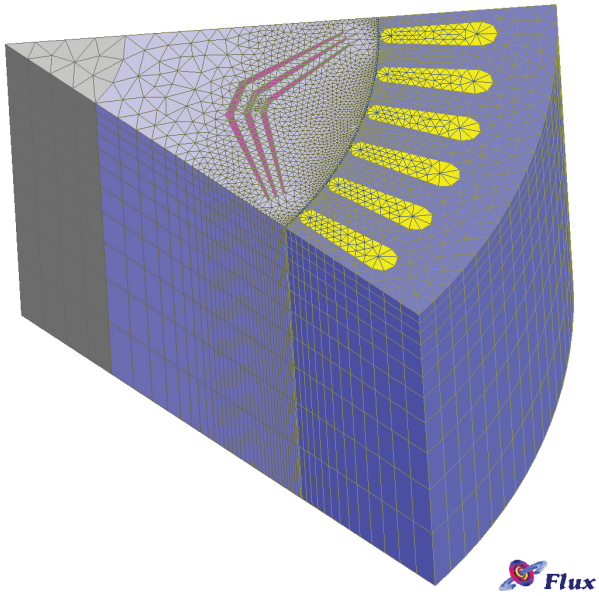

Figure 9. Mesh diagram of the simulated machine.

Figure 10 shows the distribution of the flux in prototype No. 3. As discussed in the above sections, in this study, flux lines are circumferential at the center of the pole and the distances between the PM and air gap for all of the Interior-PMSM designs. Figure 11 shows the isovalue diagram of the flux density at the rated power for prototype No. 3. For all of the prototypes in this study, the maximum flux density is less than the saturation flux density of the permendur and close to the saturation point of this material, but the flux density value of each prototype is different.

The air gap flux density over a predefined path (for 4 poles) is shown in Figure 12a at the rated power for prototype No. 3 and this predefined path is shown in Figure 12b.

The back EMF for one phase of prototype No. 3 is shown in Figure 13, where the RMS value of the back EMF per phase must be equal to the RMS value of the input voltage per phase. Now, by changing the type of PM and temperature, the variation of the output quantities is investigated.

From Eq. (1), it is obvious that B_r and H_c reduction leads to higher volume of the PM. In this study, for this motor, using bonded Sm_2Co_{17} (motor prototype No. 1), 10,636 cm^3 of the rotor volume must be PM,

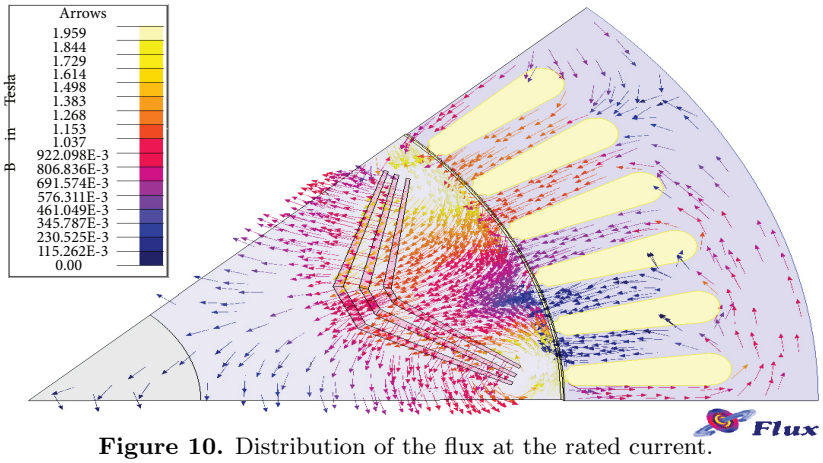

Figure 10. Distribution of the flux at the rated current.

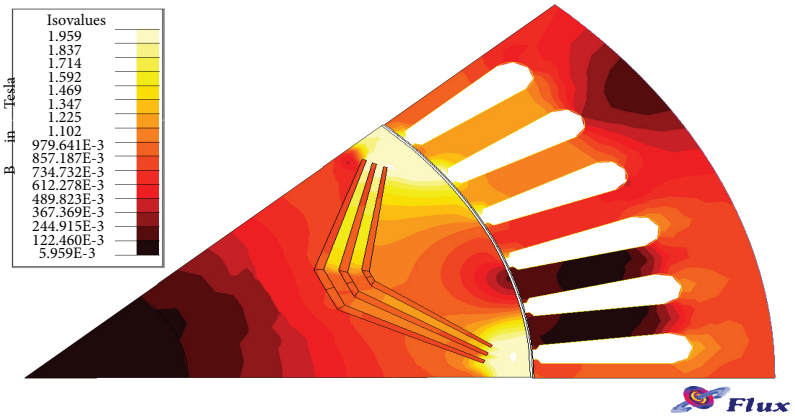

Figure 11. Isovalues of the flux density at the rated current.

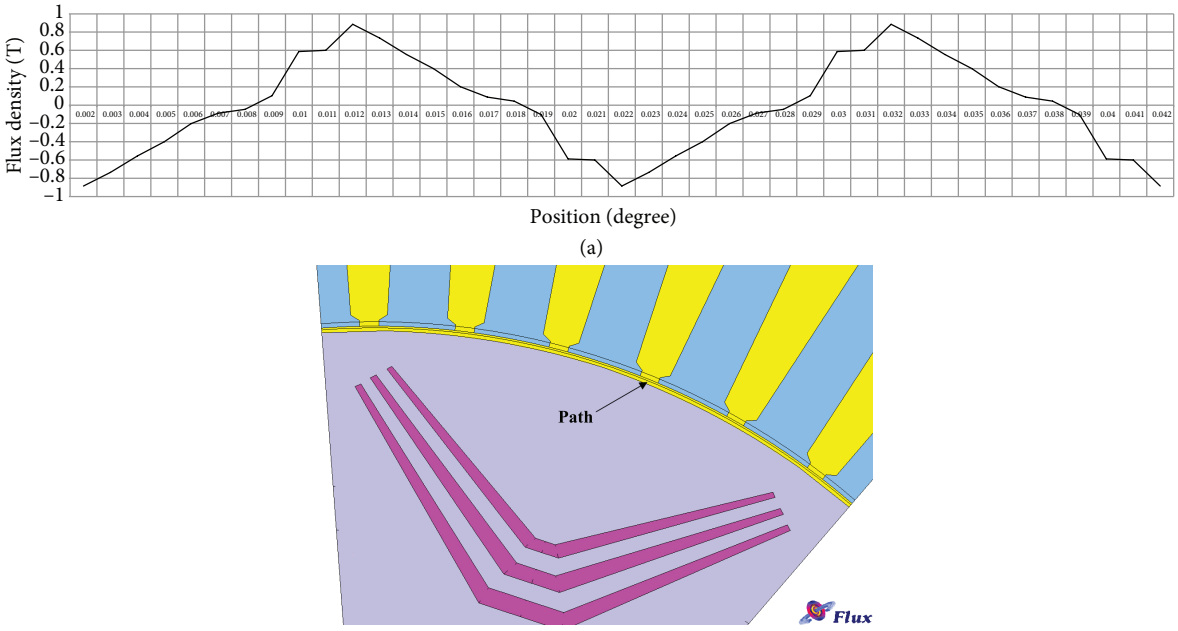

Figure 12. a) Air gap flux density diagram over the path (for 4 poles); b) air gap path belonging to a pole.

and using bonded Nd-Fe-B (motor prototype No. 2), 11,914 cm^3 of this kind of PM must be used in the rotor structure to attain the required back-EMF. If sintered Sm_2Co_{17} is used (motor prototype No. 3), 7488 cm^3 of this kind of PM must be used, and, finally, using sintered Nd-Fe-B (motor prototype No. 4), the minimum volume of the PM (5980 cm^3) of the rotor volume must be used to attain the required back-EMF.

Table 4 demonstrates the variations of the power factor versus the PM type, and the damaging effect of increasing the temperature on the power factor is also shown in this diagram.

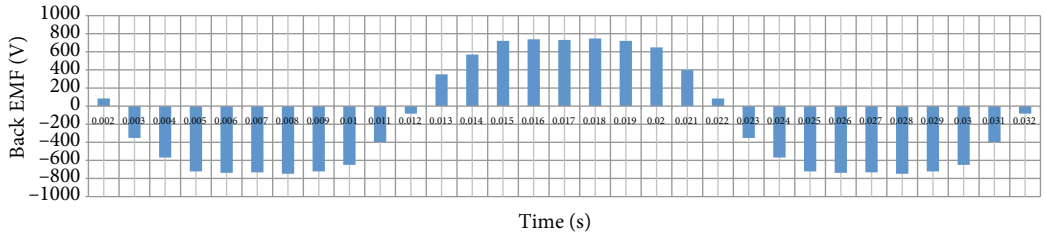

Figure 13. Back EMF for phase a.

Figure 14 demonstrates the variations of the cogging torque versus the PM type, as well as the effect of increasing the temperature on the cogging torque. Figure 14 also shows that with this structure (trapezoid-form fragmental buried magnet), the cogging torque for all of the prototypes is less than 2.4% of the rated torque, but the cogging torque in conventional Interior-PMSMs is about 5% of the rated torque. By increasing the volume of the PM, the cogging torque will be increased.

Table 4. Variation of the power factor versus the PM temperature.

Parameters	25 °C	85 °C	155 °C	175 °C	300 °C
Prototype No. 1	94%	91.9%	-	-	-
Prototype No. 2	93.7%	88.8%	87.3%	-	-
Prototype No. 3	96.5%	93.5%	91.2%	88%	83.5%
Prototype No. 4	98%	97%	95.2%	94.5%	-

The cogging torque is the consequence of the interaction (magnetic attraction) between the rotor-mounted PMs' field and the stator teeth, which produces reluctant variations on the rotor position; it is stator current-independent. It manifests itself by the rotor's tendency to align with the stator in a number of stable positions (where the permeance of the PMs' magnetic circuit is maximized), even when the machine is unexcited, resulting in a pulsating torque, which does not contribute to the net effective torque. Optimizing the cogging torque to a low value can allow a low torque ripple and harmonic reduction to be obtained [12–14].

The torque per ampere diagrams for all of the prototypes are shown in Figure 15, where by increasing the inductance of the excitation axis that is achieved by increasing of the volume of the PM in the rotor structure, the torque per ampere diagram will be improved.

The effect of different PM types and temperatures on the torque per rated current is shown in Figure 16, where with improvement of the PM hysteresis loop characteristics, the inductance of the excitation axis and torque per ampere will be increased. The variation of the excitation axis inductance by the PM hysteresis loop characteristics variation can be proven through Eqs. (2)–(4) and Figures 6–8. Figure 17 shows the CPSR diagram for prototype No. 3, and the CPSR is obtained by (see [1,5,12]):

$$CPSR = \frac{\omega_{\max}}{\omega_{rated}}. \tag{5}$$

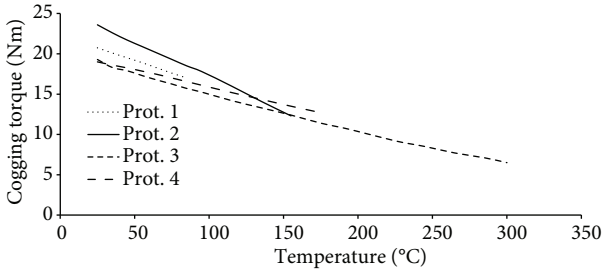

Figure 14. Cogging torque variations versus the temperature of the PM.

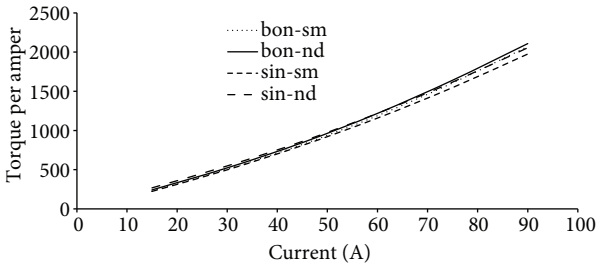

Figure 15. Torque per ampere diagram at 25° C.

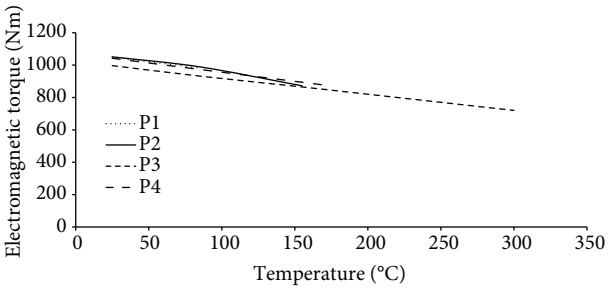

Figure 16. Effect of temperature and PM type on the steady-state torque value.

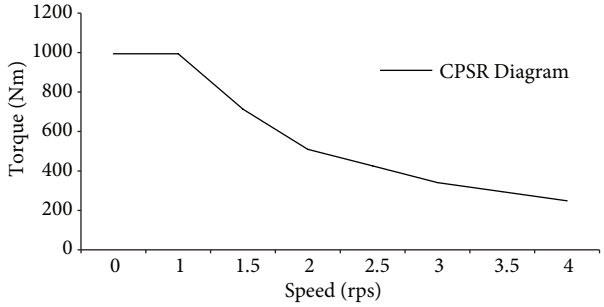

Figure 17. CPSR versus PM type.

CPSR is quite dependent on the field weakening operation in Interior-PMSMs, i.e. the field weakening operation will be improved by increasing the inductance of the excitation axis [5]. By analysis of the CPSR diagram, it can be seen that the CPSR in all of the cases is up to 4 and the performance of the machine in the constant power area of this diagram shows the advantage of this novel structure.

7. Conclusion

In this paper, for an accurate analysis of the Interior-PMSM and to perform the sensitive analysis for this motor, a finite element analysis model is used. A hysteresis loop in an inclined rhombus shape is adapted for the analysis of the hysteresis loop. A simulation based on the real dimensions of a typical Interior-PMSM is performed. The back EMF, power factor, cogging torque, flux density, torque per ampere diagram, and CPSR are then presented considering different PM types. Furthermore, the effect of temperature variation on the PM hysteresis loop characteristics is investigated and the variation of these output quantities versus the PM temperature is extracted. All of the simulation results verify the improvement of the Interior-PMSM performance using sintered Nd-Fe-b materials, such as a) less volume of the PM and cogging torque, b) best torque per ampere diagram, and c) good power factor. Unfortunately, the temperature analysis shows the damaging effect of increasing the temperature on different parameters of the machine, such as the machine's power factor, steady-state torque value, etc. These are specific when Nd-Fe-b materials are in use. In other words, it can be observed that B_r increases or μ_r decreases will improve the motor output characteristics like electromagnetic torque per ampere, linkage flux between the rotor and stator, power factor, etc., but the cogging torque and torque ripple will be increased.

References

[1] J. Soleimani, A. Vahedi, S.M. Mirimani, "Inner permanent magnet synchronous machine optimization for HEV traction drive application in order to achieve maximum torque per ampere", Iranian Journal of Electrical and Electronic Engineering, Vol. 7, pp. 241–248, 2011.

[2] R.H. Staunton, S.C. Nelson, P.J. Otaduy, J.W. McKeever, J.M. Bailey, S. Das, R.L. Smith, PM Motor Parametric Design Analyses for a Hybrid Electric Vehicle Traction Drive Application, Oak Ridge, TN, USA, Oak Ridge National Laboratory, US Department of Energy, 2004.

[3] Y. Fujishima, S. Wakao, M. Kondo, N. Terauchi, "An optimal design of interior permanent magnet synchronous motor for the next generation commuter train", IEEE Transactions on Applied Super Conductivity, Vol. 14, pp. 1902–1905, 2004.

[4] Y. Honda, T. Nakamura, T. Higaki, Y. Takeda, "Motor design considerations and test results of an interior permanent magnet synchronous motor for electric vehicles", Conference Record of the IEEE Industry Applications Conference 32nd IAS Annual Meeting, pp. 75–82, 1997.

[5] J. Soleimani, A. Vahedi, A. Ejlali, "New structures of IPM machine for HEV traction: investigation on field weakening performance and harmonic analyzing", International Review of Electrical Engineering, Vol. 6, pp. 2310–2317, 2011.

[6] J.E. Gould, "Permanent magnet applications", IEEE Transactions on Magnetics, Vol. 5, pp. 812–821, 1969.

[7] W.L. Soong, N. Ertugrul, "Field-weakening performance of interior permanent-magnet motors", IEEE Transactions on Industry Applications, Vol. 38, pp. 1251–1258, 2002.

[8] A. Wang, H. Li, C.T. Liu, "On the material and temperature impacts of interior permanent magnet machine for electric vehicle applications", IEEE Transactions on Magnetics, Vol. 44, pp. 4329–4332, 2008.

[9] J. Soleimani, A. Vahedi, "3-Phase surface mounted PMSM improvement considering hard magnetic material type", International Journal of Advanced Engineering Sciences and Technologies, Vol. 7, pp. 36–41, 2011.

[10] M.S. Widyan, Design, Optimization, Construction and Test of Rare-Earth Permanent-Magnet Electrical Machines with New Topology for Wind Energy Applications, PhD, Department of Electrical and Computer Engineering, Technical University of Berlin, 2006.

[11] D.K. Woo, S.Y. Lee, J.H. Seo, H.K. Jung, "Optimal rotor structure design of interior-permanent magnet synchronous machine base on improved niching genetic algorithm", 18th International Conference on Electrical Machines, pp. 1–4, 2008.

[12] Y. Honda, T. Higaki, S. Morimoto, "Rotor design optimisation of a multi-layer interior permanent-magnet synchronous motor", IEE Proceedings - Electric Power Applications, Vol. 145, pp. 119–124, 1998.

[13] J.A. Guemes, A.M. Iraolagoitia, J.I.D. Hoyo, P. Fernandez, "Torque analysis in permanent-magnet synchronous motors", IEEE Transactions on Conversion, Vol. 26, pp. 55–63, 2011.

[14] A. Yamada, H. Kawano, I. Miki, M. Nakamura, "A method of reducing torque ripple in interior permanent magnet synchronous motor", Power Conversion Conference, pp. 322–325, 2007.

[15] E.S. Hamdi, Design of Small Electrical Machines, New York, NY, USA, Wiley, 1995.

[16] Armco Steel Corporation, The Metallurgy of Iron and Silicon-Iron for Soft Magnetic Applications, Technical Report, Middletown, OH, USA, Armco, 2011.

[17] J.F. Gieras, Permanent Magnet Technology, Design and Application, London, UK, Marcel Dekker Inc., 2002.

[18] C.M. Ong, Modeling and Dynamic Simulation of Electric Machinery, Upper Saddle River, NJ, USA, Prentice Hall, 1998.

[19] A. Consoli, G. Renna, "Interior type permanent magnet synchronous motor analysis by equivalent circuit", IEEE Transactions on Energy Conversion, Vol. 4, pp. 681–689, 1989.

[20] A.H. Wijenayake, P.B. Schmidt, "Modeling and analysis of permanent magnet synchronous motor by taking saturation and core loss into account", International Conference on Power Electronics and Drive Systems, Vol. 2, pp. 530–534, 1997.

[21] V.B. Honsinger, "Performance of polyphase permanent magnet machines", IEEE Transactions on Power Apparatus and Systems, Vol. 99, pp. 1510–1518, 1980.